ACS Catalysis

Open Access
This article is licensed under CC-BY 4.0

pubs.acs.org/acscatalysis
Research Article

Disentangling Plasmonic Enhancement of Electronic and Thermal Effects in Catalysis Using In Operando X-ray Diffraction

Rebeca Miyar, Ieng Wai Un, Shani Har Lavan, Yonatan Dubi, Joshua H. Baraban, Yonatan Sivan, and Brian A. Rosen*

Cite This: ACS Catal. 2025, 15, 2359−2366
Read Online

ACCESS | Metrics & More | Article Recommendations | Supporting Information

ABSTRACT: Photocatalysis by illumination of plasmonic catalytic nanostructures may offer energetically efficient and highly selective alternatives to state-of-the-art thermocatalysis, which typically requires significant energy input for a high temperature operation. While many demonstrations of plasmonic photocatalysis exist, disagreement remains regarding the mechanism(s). Originally, nonthermal (so-called "hot") carriers appeared responsible for the catalysis, but recently heating emerged as a likely primary mechanism. Distinguishing between these two mechanisms is difficult since it requires accurate knowledge of the catalyst temperature. Here, we report in operando X-ray diffraction under illumination to unambiguously determine the average temperature of the catalyst during CO oxidation by measuring lattice parameters of both the catalytic nanoparticles and their oxide support. By simultaneously measuring the reaction rate, we find that "hot" carriers play no role in this reaction with this catalyst. Our experimental design provides a generally applicable method for the determination of the catalytic mechanism and paves the way for future chemical studies of catalytic plasmonic nanostructures.

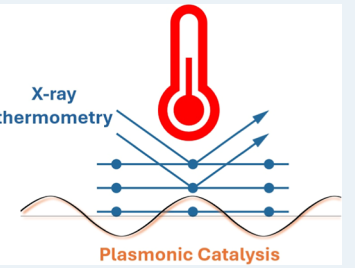

KEYWORDS: *X-ray thermometry, CO oxidation, hot carrier, plasmons, thermal catalysis*

Downloaded via 79.177.139.167 on January 25, 2025 at 16:54:14 (UTC).
See https://pubs.acs.org/sharingguidelines for options on how to legitimately share published articles.

INTRODUCTION

Contemporary environmental challenges call for innovation in chemistry and energy. One appealing idea is solar-powered photocatalysis by earth-abundant metal nanoparticles (MNPs), taking advantage of renewable resources for green chemistry while reducing the material and power requirements. The original mechanism proposed for photocatalysis by MNPs was "hot carrier" generation, wherein illumination excites surface plasmons that energize nonthermal (colloquially but imprecisely known as "hot") carriers, which were thought to drive desired reactions.[1−23]

However, when MNPs are illuminated, they also heat up,[24−34] a fact which raises a natural and fundamental question: can one distinguish between "hot" carrier catalysis and thermocatalysis (i.e., reaction rate increases at elevated temperatures)? This question, combined with the observation of ultrafast thermalization time of excited carriers in MNPs and the resulting minuscule occupation of high energy carrier states,[35−37] prompted an ongoing debate as to the true origin(s) of MNP photocatalysis.[19,23,37−40] Dissecting the potentially complex behavior of photocatalytic MNPs via these two distinct mechanisms is essential for understanding the underlying physics of "hot carrier" catalysis and optimizing possible uses in energy and environmental applications.

Two critical obstacles for differentiating "hot carrier" from thermal catalysis are the macroscopic (i.e., millimeter/centimeter scale) thermal nonuniformities and the accuracy of the catalyst temperature measurement. The first obstacle, relevant in particular for optically thick samples necessary to harvest all incident light, typically exhibit linear axial gradients[32,39,41,] as well as transverse gradients even if the sample is illuminated uniformly; these gradients can mislead as to the underlying mechanism of the catalyzed reaction.[23,36−40] To solve this issue, the sample geometry can be optimized to be thin enough to minimize thermal gradients but thick enough to still harvest a sufficient portion of light. Importantly, microscopic temperature gradients in the catalyst layer induced by mass transfer limitations coupled with the enthalpy of reaction cannot always be remedied by optimizing sample geometry.

The second, more challenging obstacle refers to the accuracy of the temperature measurement itself. Prior experimental thermometry work relied on thermocouples or thermal cameras to probe the catalyst temperature, but limitations of these techniques have prevented them from achieving consistent and therefore conclusive data. Furthermore, poor thermal contact between thermocouples and the sample surface is a source of error, a problem that is particularly challenging for thin films.[42] Potential alternative high quality

Received: November 6, 2024
Revised: January 18, 2025
Accepted: January 20, 2025

ACS Publications
© XXXX The Authors. Published by American Chemical Society

https://doi.org/10.1021/acscatal.4c06841
ACS Catal. 2025, 15, 2359−2366

temperature measurement techniques such as fluorescence-based thermometry,[43,48] or anti-Stokes photoluminescence from the MNPs themselves,[49,50] or from semiconducting nanocrystals,[51] have not been applied to plasmon-assisted photocatalysis experiments to date. Finally, the popular approach of surface-enhanced Raman spectroscopy (SERS)[42,53−55] involve complex calibration of the temperature reading due to the unequal and space-dependent enhancements of the Stokes and anti-Stokes peaks by the plasmon-induced near-field.[19,52]

Since in plasmonic photocatalytic chemistry there is sometimes inaccurate knowledge of the plasmonic catalyst temperature, here we present an X-ray diffraction (XRD)-based experimental technique that can monitor photocatalysis in MNPs and simultaneously unambiguously determine the average temperature of the catalyst itself. Since the technique measures the average temperature, we further apply an optimized sample geometry to minimize macroscopic thermal gradients. This technique is applied to CO oxidation on a thin film sample of Cu/Ru antenna/active-site catalyst similar to that reported previously in the literature.[22] By carefully establishing the catalyst and support temperatures in the dark and under illumination while simultaneously measuring the corresponding reaction rates, we find that for this reaction, under these conditions, there is no evidence of "hot carrier" catalysis. Importantly, this method can be applied to a variety of systems and reactions, thus promoting our understanding of plasmonic photocatalytic systems.

RESULTS AND DISCUSSION

The potential involvement of plasmon-enhanced catalytic activity by electronic and thermal effects in CO oxidation was studied by using Cu−Ru NPs supported by a composite ceramic of aluminum oxide and magnesium oxide (Cu−Ru/Al_2O_3−MgO). Similar catalyst configurations have been used previously for studying plasmon-enhanced catalysis by exploiting the plasmonic properties of nanoscale Cu (i.e., the antenna) doped with a low concentration of Ru,[22] a well-known active site for CO oxidation.[56] XRD in Figure S1 shows only Cu and crystalline MgO, meaning that Al_2O_3 in the supporting oxide was amorphous. Ru is present as a low concentration alloying metal in the Cu NPs and is not discernible by diffraction. Inductively coupled plasma with optical emission spectroscopy (ICP-OES) measured the Cu/Ru ratio of the catalyst to be 50:1. The presence of Ru was further confirmed by X-ray photoelectron spectroscopy (XPS) (Figure S2). High-angle annular dark field (HAADF) transmission electron microscopy (TEM) was used to measure the $Cu_{50}Ru_1$ particle size distribution. Characteristic HAADF images of supported CuRu particles (Figure S3) gave an average particle size of about 30 nm. The Ru content was too low in order to be reliably detected by electron-dispersive X-ray spectroscopy (EDX) elemental mapping. The CuRu@MgO/Al_2O_3 catalyst was mixed with a commercial binder, solvent, and stabilizer (Fiaxell SOFC Technologies) to form an ink and then screen-printed as an 8 mm diameter circle on a doubly polished zero-degree (C-phase) sapphire support. The binder, solvent, and stabilizer, meant only to stabilize the catalyst ink for screen printing, were all removed from the sample upon sintering at 873 K, leaving behind only the CuRu@MgO/Al_2O_3. Cross-sectional scanning electron microscopy (SEM) shown in Figure S4 was used to measure the thickness of the catalyst per screen-printed layer, which was approximately 10 μm. The weight percent of the oxide in the film was 88.5%, and the relative density of the film was measured to be 60% (i.e., 40 vol % void).

Differentiating between nonthermal and thermal catalytic activity requires accurate measurement of the temperature of the catalyst and, by extension, the catalyst itself to be isothermal. Therefore, we selected a film thickness of 30 μm, thin enough to minimize temperature gradients (see corresponding thermal simulations in Figure 1) and allow for

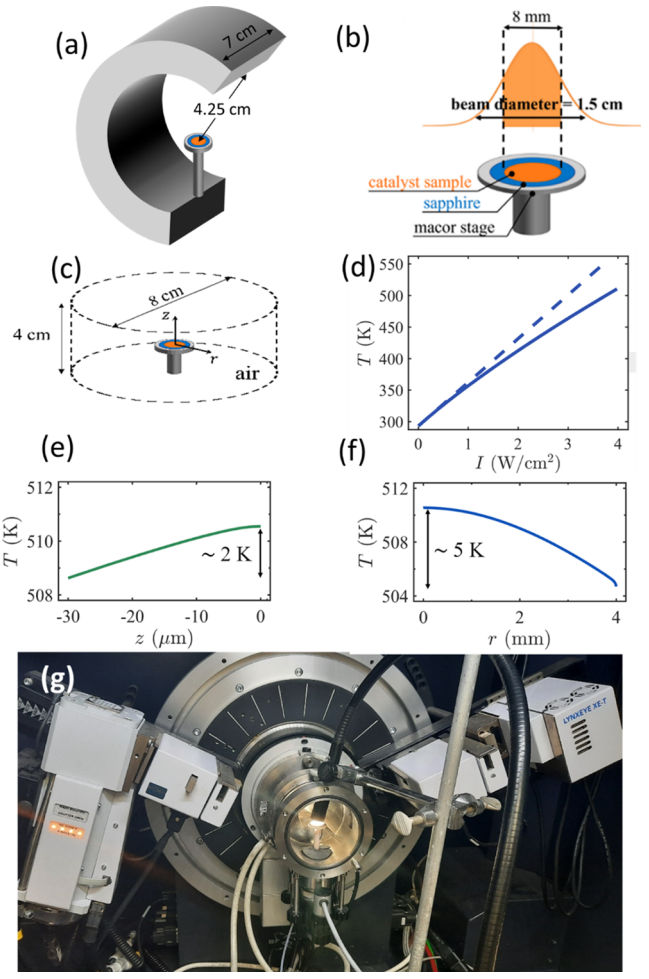

Figure 1. (a) Schematic of the simulated reaction chamber and (b) schematic of the simulated catalyst sample. (c) Simplified simulation domain for the temperature distribution calculation of the catalyst sample. (d) Simulated catalyst temperature as a function of power up to 2 W/cm^2 (a straight dashed line with the initial slope is provided to guide the eye). (e) Temperature variation throughout the catalyst layer in the axial z-direction and (f) radial r-direction under 2 W/cm^2 of white-light illumination. (g) Photograph of the in operando XRD catalytic reactor with a fed-through 8 mm diameter liquid light guide.

light penetration (Figure S5), yet thick enough that CO oxidation reaction products (CO_2) could be detected by gas chromatography with a flame ionization detector and methanizer (GC-FIDm). We simulated the temperature distribution in the catalyst sample using COMSOL Multiphysics with the effective medium approach for the absorption and accounting for the detailed reactor geometry (Figures 1a,b and S6, see details in the Supporting Information).[32,39,57] Figure 1c shows that for the source and intensity range used in our experiment, the simulations predict a linear dependence of

https://doi.org/10.1021/acscatal.4c06841
ACS Catal. 2025, 15, 2359−2366

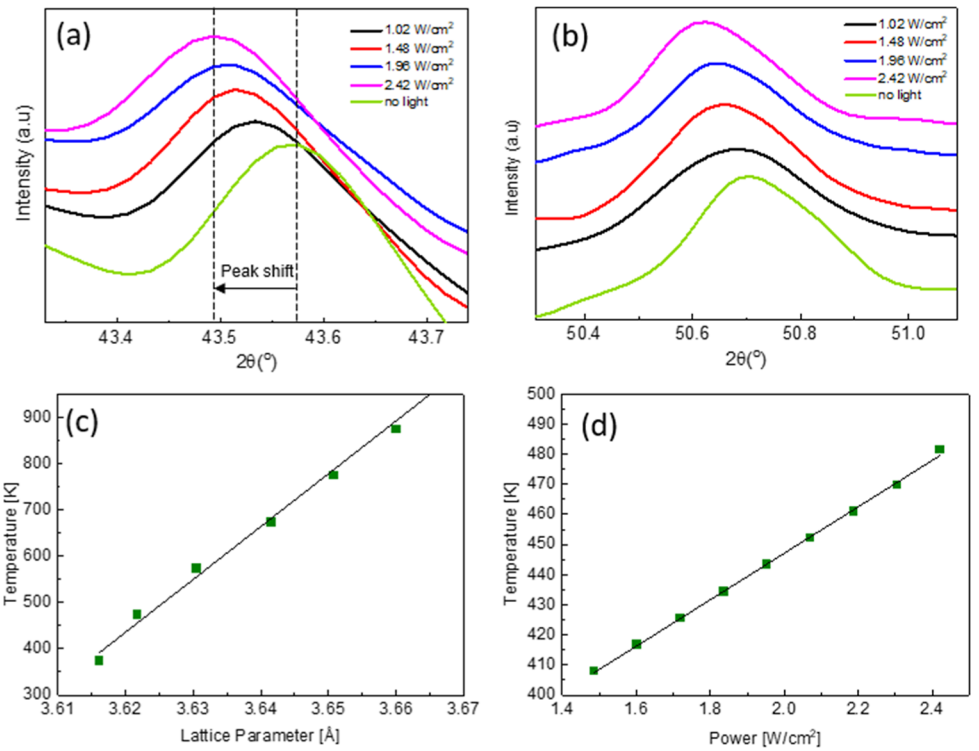

Figure 2. Selected regions of the $CuRu/Al_2O_3$−MgO catalyst diffractogram highlighting the motion of the (a) Cu(100) and (b) Cu(200) Bragg reflections as a function of light intensity. (c) Cu lattice parameter as a function of temperature when the catalyst is heated by the oven inside of the in situ reaction chamber. (d) Cu temperature as a function of light intensity. Error bars for subfigures (c,d) are significantly smaller than the icon size along both axes.

the temperature with the incident power at a rate of 68 K·cm^2/W. A weak nonlinearity associated with the temperature-dependence of the thermal conductivity of the gases (1% CO; 19% O_2; and 80% N_2) can be observed for T > 400 K, as expected.[47] Figure 1d,e shows that at 2 W/cm^2 of illumination, with an ambient temperature of 298 K, the temperature variances in the radial and axial directions were only 5 and 2 K (i.e., 0.9 and 0.4% variation), respectively, justifying the selected catalyst geometry.

The temperature of the catalyst was unambiguously determined by using in operando XRD with a modified Anton Parr XRK-900 reaction chamber fitted with a fed-through 8 mm liquid light guide (Lumatec Series 380 UVEXS). The output of the fiber-coupled white light source (EK-1, Euromex, spectral output shown in Figure S7) was matched to the sample size by using a collimator, and the power was characterized with a broadband meter (Ophir StarBright and 3A). The diffractometer acted as a temperature probe since the temperature of materials can be tracked by thermal expansion via their lattice parameter(s). Indeed, the positions of the Cu(111) and Cu(200) peaks shifted to lower angles as the light intensity was increased from 0 to 2.42 W/cm^2 as a direct result of heating under illumination (Figure 2a,b). The lattice parameter for the Cu was determined by Rietveld refinement from 2θ between 42 and 52° (Figure S8).

The relationship between the lattice parameter (peak position) and temperature was measured separately by operating the XRK-900 diffraction chamber in its unmodified oven-heated configuration under an inert atmosphere. While Rietveld refinement is typically applied to a larger 2θ range, this technique successfully fit the profile of the Cu reflections and gave a temperature vs lattice parameter relationship for Cu (Figure 2c) in agreement with previously reported literature values.[58] This agreement suggests that there are no nanoscale or strain-related contributions toward the behavior of the thermal expansion of the Cu, and that the supported 30 nm Cu particles behaved crystallographically as bulk Cu. Importantly, even if this technique was applied to a strained or defective catalyst that did not behave as its bulk counterpart, these behaviors would be captured in Rietveld refinement during the thermal calibration stage. Application of the thermal calibration curve to the diffractograms collected as a function of light intensity allowed calculation of the Cu temperature under illumination (Figure 2d). The slope of this curve is 77 K·cm^2/W, in relatively good agreement with the 68 K·cm^2/W predicted by simulation (Figure 1c).

Previous reports tracked the temperature of the catalyst using a thermal camera or thermocouple. A thermocouple cannot be used to differentiate between the temperatures of different phases in the nanoscale catalyst, and present other well-known measurement challenges in high-temperature small-scale scenarios.[37,39,59] Thermal cameras are entirely dependent on accurate knowledge of the sample's emissivity, which is often unknown and different for each phase in the sample. In fact, our extended calculation of the absorptivity (Figure S9 and accompanying text) reveals a strong wavelength dependence of the emissivity, which further demonstrates the unsuitability of a thermal camera for this class of samples.[23,38] We note in passing that our attempts to use a thermal camera required that the sample emissivity be set to 0.25 before the catalyst temperature recorded by the thermal camera matched that of the diffractometer (Figure 3a) or a thermocouple. By contrast, the in operando XRD method can be used to unambiguously determine the temperature of each crystalline

https://doi.org/10.1021/acscatal.4c06841
ACS Catal. 2025, 15, 2359−2366

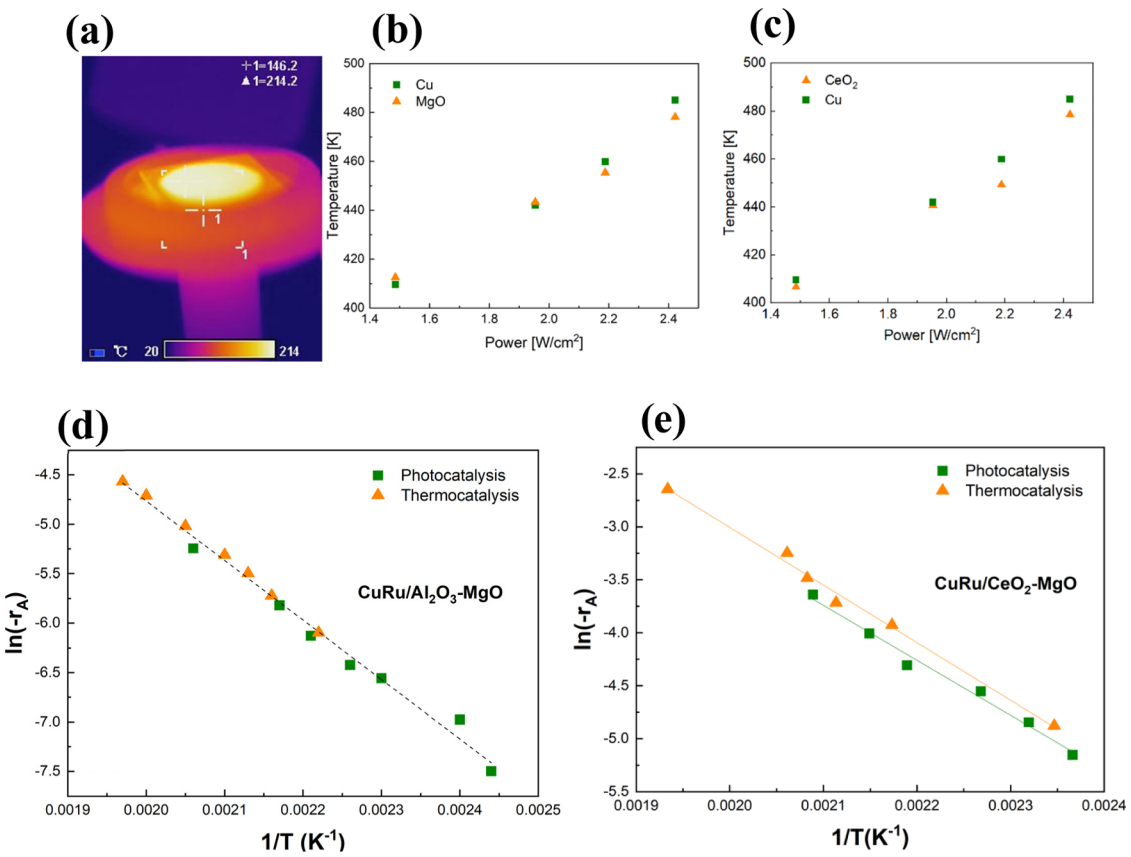

Figure 3. (a) Catalyst temperature profile taken by a thermal camera with emissivity setting set to 0.25. Circular catalyst layer is screen-printed onto a square sapphire support, which itself was placed on a Macor sample stage inside of the in operando XRD chamber. (b) Temperature of MgO and Cu in the CuRu/Al_2O_3−MgO catalyst under illumination as determined by in operando diffraction. (c) Temperature of CeO_2 and Cu in the CuRu/CeO_2−MgO catalyst under illumination as determined by in operando diffraction. (d) Arrhenius plot for CO oxidation over a CuRu@MgO/Al_2O_3 film where the temperature in the thermocatalytic analogue experiment was selected to be in the same range as the temperatures observed in the photocatalytic experiment using in operando XRD. Error for each point is the size of the data point itself. (e) Temperature of CeO_2 and Cu in the CuRu/CeO_2−MgO catalyst under illumination as determined by in operando diffraction using the same geometry and configuration as the CuRu/Al_2O_3−MgO. Error for each point is the size of the data point itself.

phase in the catalyst during the reaction itself. This differentiates the method from potential alternatives for high-quality temperature mapping such as SERS,[53−56] fluorescence-based thermometry,[43−48] or anti-Stokes photoluminescence from the MNPs themselves,[49,50] or from semiconducting nanocrystals.[52] Simulations of the temperature difference between the Cu and the crystalline Al_2O_3−MgO yielded less than 12 mK (Figure S10), in agreement with earlier work,[24,33] justifying our assumption that the temperature of the Cu represents the temperature of the oxide support. Importantly, differences in the temperature between the metal and ceramic support would not be detected by using alternative thermometry techniques. To verify these simulations, in operando diffraction was again used to obtain the temperature of the ceramic support, thus providing a first of its kind thermometry technique that can also provide information on nanoscale temperature differences between the particles and their immediate surroundings. XRD showed agreement between the Cu and MgO temperatures to within 2 K below 2 W/cm^2 and to within 5 K up to 2.42 W/cm^2 (Figure 3b), which is an ∼1% deviation. For additional verification, an alternative catalyst was made in which the amorphous Al_2O_3 was replaced with crystalline CeO_2 (i.e., a CuRu/CeO_2−MgO). In operando diffraction for this sample again showed agreement between the Cu and CeO_2 temperatures to within 2 K below 2 W/cm^2 and to within 5 K up to 2.4 W/cm^2 (Figures 3c and S11). Intriguingly, the temperature difference between the Cu metal and its oxide support (Figure 3b,c) is quite small, albeit still higher than that predicted by simulations (Figure S10). Although most catalyst samples (including the presently reported catalyst) are predicted to have a negligible temperature gradient between the MNP and catalyst support, Kamarudheen et al.[60] has shown that in MNP arrays with large interparticle distances relative to the NP size and sufficiently strong illumination, a much greater temperature difference can be achieved between the particle and average background temperature (i.e., a microscopic gradient). Future catalysts designed as NP arrays could therefore benefit from X-ray thermometry.

With accurate monitoring of the sample temperature, the performance of the CuRu/Al_2O_3−MgO and CuRu/CeO_2−MgO photocatalysts for the CO oxidation reaction was investigated by measuring the reaction rate vs temperature under illumination. In order to justify the attribution of the Cu diffraction peak shifts only to temperature (and not to bulk oxidation), the valence state of the Cu surface *after* photothermal catalysis was studied by XPS. Differentiating between Cu and CuO using conventional XPS is straightforward since there is an ∼2 eV shift in the $2p_{3/2}$ binding energy to higher values upon oxidation. XPS in Figure S12a shows the

https://doi.org/10.1021/acscatal.4c06841
ACS Catal. 2025, 15, 2359−2366

Cu 2p peak appearing at 932.1 eV, which is in line with metallic Cu and/or Cu_2O and not high enough for the fully oxidized CuO, whose peak appears closer to 934.6 eV.[61] Multiple effects make differentiating between Cu and Cu_2O difficult using XPS, and therefore Auger spectroscopy on the Cu LM2 transition was measured (Figure S12b) as a method to differentiate between Cu and Cu_2O. The Cu LM2 transition was measured at 917.1 eV. The LM2 peak for metallic Cu and Cu_2O can be found at 918.6 and 916.6 eV,[62] respectively. From this, we can conclude that the surface of the NPs is a mixture between Cu and Cu_2O. Furthermore, XRD of the catalyst was taken after reaction and cooling down to room temperature, and Cu peaks returned to their original position, ruling out bulk Cu-oxidation.

While the use of Cu for oxidation reactions can be complex owing to the tendency of metallic Cu to oxidize under thermal conditions, Marimuthu et al.[63] have previously shown that localized surface plasmons formed on Cu NPs have a reducing effect by weakening Cu−O bonds, and act to partially prevent overoxidation (i.e., limit the formation of Cu_2O and prevent CuO). Previous studies have shown that Cu_2O gives plasmonic response[64,65] and has been studied for catalytic applications including plasmonic behavior.[63,66]

An Arrhenius plot was constructed by plotting the logarithm of the reaction rate against the reciprocal temperature. Critically, the temperature used for the abscissa in the Arrhenius plot and activation energy calculation is the one measured by the in operando diffraction. The analogous thermocatalytic control experiment, enabled by the minimization of temperature gradients across the small sample, was carried out using the exact same catalyst placed inside a single-ended quartz tube with the same volume as the X-ray reaction (Figure S13) and the expected thermal uniformity (Figure S14). The tube was placed inside a muffle furnace, and the CO oxidation activity was recorded on the same catalyst configuration in a similar temperature range as determined by the diffraction in the operando photocatalytic experiment.

Figure 3d shows that for the $CuRu/Al_2O_3$−MgO catalyst, there is little to no difference in the activation energy for the light-driven (47 ± 2 kJ/mol) and thermally driven reactions (51 ± 2 kJ/mol). Similarly, for the $CuRu/CeO_2$−MgO variant, the activation energies for the light-driven (43 ± 2 kJ/mol) and thermally driven reaction (45 ± 2 kJ/mol) agreed with each other to within the experimental uncertainties (Figure 3e). The experiments were repeated 3 times, with a fresh catalyst used for each experiment. In the case of supported CuRu catalysts for CO oxidation, it was therefore observed that when the temperature is measured by in operando diffraction, there is indistinguishable photocatalytic activity from the thermally driven analogue.

CONCLUSIONS

This work focused on the simultaneous and unambiguous determination of the catalyst temperature and reaction rate during plasmonic reactions with a specific example from CO oxidation. Our success in such a unified measurement demonstrates a new platform for careful analysis of reaction mechanisms in plasmonic-enhanced reactions and offers a new path for understanding the critical ingredients and physical mechanisms for plasmonic photocatalysis as well as enabling the reliable testing of the potential of plasmonic catalysis for improving reaction efficiency and selectivity. While in this work, the X-ray beam dimensions were matched to the sample area and therefore not used to map the temperature of the sample, the methodology presented here can be extended to microfocused XRD beams enabled by synchrotron radiation, allowing for spatial (mapping) and temporal resolution.

METHODS

$CuRu/MgO-Al_2O_3$ Catalyst Synthesis. 0.7176 g $Cu(NO_3)_2{\cdot}3H_2O$ (STREM Chemicals, catalog no. 93239, 99.5%) and 7.84 mg $RuCl_3{\cdot}3H_2O$ (Alfa Aesar, catalog no. 11043, 99.9%) were dissolved with 2.308 g $Mg(NO_3)_2{\cdot}6H_2O$ (STREM Chemicals, catalog no. 931238, 99.0%) and 1.125 g $Al(NO_3)_2{\cdot}9H_2O$ (Alfa Aesar, catalog no. 12360, 98.0%) in 15 mL deionized (DI) water to create the metal precursor solution. Another solution was made by dissolving 2.544 g of anhydrous Na_2CO_3 (MERCK, catalog no. 497198, 99.9%) in 20 mL of DI water. To a 3-neck, round flask, 10 mL of DI water was added and heated to 353 K. The metal precursor solution and basic solution were added simultaneously, in a dropwise manner, to the preheated water. The pH was monitored with a pH meter and kept at 8 by varying the speed of addition of both solutions. The resulting solid slurry was stirred at 353 K for 24 h before cooling to room temperature. The catalyst precursor was isolated by centrifuging the slurry and subsequently washed 4 times with DI water and dried in the air at 393 K for 12 h. The dry precursor was put in a tube furnace and purged with 200 sccm He (294 K) for 30 min. It was then heated to 873 K, with a ramp rate of 10 K/min, and held for 1 h in 20 sccm He, proceeded by an hour of reduction in 10 sccm H_2 at 873 K.

Catalyst Specimen Preparation. Ink was prepared composed of the CuRu surface alloy catalyst described above, a dispersant, and binder (Fiaxell). The specimen consisted of 3 layers with 313 K drying between the screen-printing process of each individual layer. The diameter of the anode was fixed at 8 mm. The sample was held in a furnace at 573 K for 2 h. Subsequently, it was sintered at 873 K for 1 h under H_2 flow of 200 sccm to allow for sintering of the specimen without allowing oxidation of the Cu NPs.

In Situ Temperature Measurements. The temperatures of the printed catalyst under illumination were evaluated by XRD (D8 Advance, Bruker AXS Madison, WI, USA) with Bragg−Brentano geometry and a Cu Kα radiation source. The printed catalyst sample was placed on a Macor sample stage in a modified Anton Paar XRK-900 reaction chamber. The chamber was modified to fit an 8 mm liquid light guide (LLG Series 380 UVEXS, Lumatec) and a collimator to illuminate the sample. The LLG was connected to a Cold Light Illuminator EK-1 light source (Euromex Resources Ltd.) containing a 100 W halogen light source. The chamber itself has an inlet for feed gas and an outlet connected to a GC (Multiple Gas Analyzer #5, SRI Instruments). The diffraction pattern was recorded from 2θ = 30 to 60° (main Cu peaks). Data points were acquired in increments of 0.02° and an acquisition time of 10 s. The lattice parameter was fitted by Rietveld refinement using TOPAS software version 5 (Bruker AXS, Madison, WI, USA). Patterns were acquired at different illumination powers (0 and 0.7−1.2 W/cm^2), and when changing the light source's power, there was a 15 min dwell time before taking a new set of measurements. The change in the catalyst temperature via illumination was measured by calibrating the lattice parameter as a function of the temperature in an inert atmosphere. The calibration curve was made via in situ XRD measurements in a manner similar to

https://doi.org/10.1021/acscatal.4c06841
ACS Catal. 2025, 15, 2359−2366

the one detailed above, using the XRK chamber in standard oven-heated mode and collecting patterns for temperatures ranging from room temperature to 850 °C. The surface temperatures of the catalyst under illumination were also recorded with a thermal camera (IR-CAM-160, MRC, United Kingdom). The emissivity of the catalyst powder was set to be 0.95 initially for testing and subsequently to 0.25 for accurate readings.

Photocatalytic Measurements. Photocatalytic CO oxidation reactions were performed in a modified XRK chamber reactor with the printed catalyst. Prior to reaction, the chamber containing the catalyst was purged in 100% N_2 for 1 h, and the white light from the setup described above was focused on the catalyst. The feed gas (1 sccm CO, 20 sccm O_2, and 79 sccm N_2, all 99.999 vol %) was stabilized for 15 min. The chamber was kept at room temperature, and the catalytic reaction was carried out under atmospheric pressure. The temperature of the chamber was kept at room temperature, and all the catalytic reactions were performed under atmospheric pressure. The efflux composition was monitored by a GC (Multiple Gas Analyzer #5, SRI Instruments).

Thermocatalytic Measurements. Thermocatalytic CO oxidation reactions were performed in a 1″ quartz reactor tube with the printed catalyst placed at the bottom of the tube. The thermocatalytic reaction was carried out under the same conditions as the photocatalytic, besides temperature. The reaction temperature varied from 130 to 240 °C, the range measured for the photocatalytic reaction. The efflux composition was monitored by a GC.

Additional Characterization. Power XRD (e.g., not in operando) was performed on a Bruker AXS D8 Advance instrument with a Bragg−Brentano geometry and a Cu Kα (λ = 1.5406 Å) radiation source. Diffraction patterns were recorded from 2θ = 10° to 2θ = 100°. Data points were acquired at increments of 0.02°, an acquisition time of 0.5 s, and a sample rotation rate of 15 rpm. Phase identification was done with Bruker Diffrac.EVA software. HAADF−STEM and energy-dispersive X-ray spectroscopy (EDS) mapping were performed on a JEOL JEM-2010F STEM operated at a 200 kV acceleration voltage. XPS was performed on a 5600 Multi-Technique System. The sample was irradiated with an Al Kα monochromated source (1486.6 eV), and the outcome electrons were analyzed by a spherical capacitor analyzer using a slit aperture of 0.8 mm. Spectra were shifted to match the adventitious C 1s peak at 284.8 eV. Cleaning of the substrate was done using Ar^+ sputtering for 0.5 min on a 4 × 4 mm raster, calibrated for 47.6 A/min for SiO_2/Si. ICP−OES was performed on a PlasmaQuant PQ9000 ICP emission spectrometer to measure the mass percentages of Cu and Ru in the catalyst. Environmental SEM (ESEM) and EDS were performed on a Quanta 200 FEG ESEM instrument operated at 20 kV to measure the thickness of the printed samples.

■ ASSOCIATED CONTENT

Data Availability Statement

All catalytic experimental data presented represent experiments that were performed at least 3 times. In all cases, the variation and error did not exceed the size/thickness of the data point itself as represented on the plot. Thermal simulations were performed by COMSOL Multiphysics. Data from these simulations will be provided upon reasonable request. The simulation output files are available upon reasonable request. Parameters of the input files are described in computational methods.

Supporting Information

The Supporting Information is available free of charge at https://pubs.acs.org/doi/10.1021/acscatal.4c06841.

XRD, X-ray photoemission spectroscopy, TEM, cross-section SEM, light penetration simulation, absorption simulation, temperature distribution simulation, XRD refinement examples, absorptivity simulation, simulated Cu/oxide temperature gradient, XRD from catalyst variant with ceria support, thermal analogue reactor description, simulated transverse and axial temperature distribution for thermal analogue experiment, and summary of simulations (PDF)

■ AUTHOR INFORMATION

Corresponding Author

Brian A. Rosen − *Department of Materials Science and Engineering, Tel Aviv University, Tel Aviv 6997801, Israel;* orcid.org/0000-0002-2265-8802; Email: barosen@post.tau.ac.il

Authors

Rebeca Miyar − *Department of Materials Science and Engineering, Tel Aviv University, Tel Aviv 6997801, Israel*

Ieng Wai Un − *School of Electrical and Computer Engineering, Ben-Gurion University of the Negev, Beer-Sheva 8410501, Israel;* orcid.org/0000-0002-7156-0019

Shani Har Lavan − *Department of Chemistry, Ben-Gurion University of the Negev, Beer-Sheva 8410501, Israel;* orcid.org/0009-0002-3585-8093

Yonatan Dubi − *Department of Chemistry and Ilse Katz Center for Nanoscale Science and Technology, Ben-Gurion University of the Negev, Beer-Sheva 8410501, Israel;* orcid.org/0000-0002-8988-4935

Joshua H. Baraban − *Department of Chemistry, Ben-Gurion University of the Negev, Beer-Sheva 8410501, Israel;* orcid.org/0000-0002-4523-704X

Yonatan Sivan − *School of Electrical and Computer Engineering, Ben-Gurion University of the Negev, Beer-Sheva 8410501, Israel; Ilse Katz Center for Nanoscale Science and Technology, Ben-Gurion University of the Negev, Beer-Sheva 8410501, Israel;* orcid.org/0000-0003-4361-4179

Complete contact information is available at: https://pubs.acs.org/10.1021/acscatal.4c06841

Notes

The authors declare no competing financial interest.

■ REFERENCES

(1) Baffou, G.; Quidant, R. Nanoplasmonics for chemistry. *Chem. Soc. Rev.* **2014**, *43*, 3898−3907.

(2) Nitzan, A.; Brus, L. Theoretical model for enhanced photochemistry on rough surfaces. *J. Chem. Phys.* **1981**, *75*, 2205−2214.

(3) Chen, C.; Osgood, R. Near-field photochemical imaging of noble metal nanostructures. *Phys. Rev. Lett.* **1983**, *50*, 1705.

(4) Maillard, M.; Huang, P.; Brus, L. Silver nanodisk growth by surface plasmon enhanced photoreduction of adsorbed [Ag+]. *Nano Lett.* **2003**, *3*, 1611−1615.

(5) Tian, Y.; Tatsuma, T. Mechanisms and applications of plasmon-induced charge separation at TiO2 films loaded with gold nanoparticles. *J. Am. Chem. Soc.* **2005**, *127*, 7632−7637.

(6) Ueno, K.; et al. Nanoparticle plasmon-assisted two-photon polymerization induced by incoherent excitation source. *J. Am. Chem. Soc.* **2008**, *130*, 6928−6929.
(7) Volpe, G.; Noack, M.; Aćimović, S. S.; Reinhardt, C.; Quidant, R. Near-field mapping of plasmonic antennas by multiphoton absorption in poly (methyl methacrylate). *Nano Lett.* **2012**, *12*, 4864−4868.
(8) Clavero, C. Plasmon-induced hot-electron generation at nanoparticle/metal-oxide interfaces for photovoltaic and photocatalytic devices. *Nat. Photonics* **2014**, *8*, 95−103.
(9) Thangamuthu, M.; Raziman, T.; Martin, O. J. F.; Tang, J. W. Review-Origin and Promotional Effects of Plasmonics in Photocatalysis. *J. Electrochem. Soc.* **2022**, *169*, 036512.
(10) Kamarudheen, R.; Kumari, G.; Baldi, A. Plasmon-driven synthesis of individual metal@ semiconductor core@ shell nanoparticles. *Nat. Commun.* **2020**, *11*, 3957.
(11) Kamarudheen, R.; Castellanos, G. W.; Kamp, L. P.; Clercx, H. J.; Baldi, A. Quantifying photothermal and hot charge carrier effects in plasmon-driven nanoparticle syntheses. *ACS Nano* **2018**, *12*, 8447−8455.
(12) Yu, S.; Jain, P. K. Plasmonic photosynthesis of C1−C3 hydrocarbons from carbon dioxide assisted by an ionic liquid. *Nat. Commun.* **2019**, *10*, 2022.
(13) Yu, S.; Jain, P. K. Selective branching of plasmonic photosynthesis into hydrocarbon production and hydrogen generation. *ACS Energy Lett.* **2019**, *4*, 2295−2300.
(14) Bonn, M.; et al. Phonon-versus electron-mediated desorption and oxidation of CO on Ru (0001). *Science* **1999**, *285*, 1042−1045.
(15) Wei, Q.; Wu, S.; Sun, Y. Quantum-Sized Metal Catalysts for Hot-Electron-Driven Chemical Transformation. *Adv. Mater.* **2018**, *30*, 1802082.
(16) Dai, X.; Wei, Q.; Duong, T.; Sun, Y. Selective transfer coupling of nitrobenzene to azoxybenzene on rh nanoparticle catalyst promoted by photoexcited hot electrons. *ChemNanoMat* **2019**, *5*, 1000−1007.
(17) Xu, X.; Dutta, A.; Khurgin, J.; Wei, A.; Shalaev, V. M.; Boltasseva, A. TiN@ TiO2 core−shell nanoparticles as plasmon-enhanced photosensitizers: the role of hot electron Injection. *Laser Photon. Rev.* **2020**, *14*, 1900376.
(18) Huang, H.; et al. Unraveling surface plasmon decay in core−shell nanostructures toward broadband light-driven catalytic organic synthesis. *J. Am. Chem. Soc.* **2016**, *138*, 6822−6828.
(19) Chen, K.; Wang, H. Plasmon-driven photocatalytic molecular transformations on metallic nanostructure surfaces: mechanistic insights gained from plasmon-enhanced Raman spectroscopy. *Mol. Syst. Des. Eng.* **2021**, *6*, 250−280.
(20) Negrín-Montecelo, Y.; et al. Plasmonic photocatalysis in aqueous solution: assessing the contribution of thermal effects and evaluating the role of photogenerated ROS. *Nanoscale* **2022**, *14*, 11612−11618.
(21) Jin, R.; et al. Photoinduced conversion of silver nanospheres to nanoprisms. *science* **2001**, *294*, 1901−1903.
(22) Zhou, L.; et al. Light-driven methane dry reforming with single atomic site antenna-reactor plasmonic photocatalysts. *Nat. Energy* **2020**, *5*, 61−70.
(23) Dubi, Y.; Un, I. W.; Baraban, J. H.; Sivan, Y. Distinguishing thermal from non-thermal contributions to plasmonic hydrodefluorination. *Nat. Catal.* **2022**, *5*, 244−246.
(24) Baffou, G.; Quidant, R. Thermo-plasmonics: using metallic nanostructures as nano-sources of heat. *Laser Photon. Rev.* **2013**, *7*, 171−187.
(25) Maley, M.; Hill, J. W.; Saha, P.; Walmsley, J. D.; Hill, C. M. The Role of Heating in the Electrochemical Response of Plasmonic Nanostructures under Illumination. *J. Phys. Chem. C* **2019**, *123*, 12390−12399.
(26) Lear, B. J.; Haas, K. Understanding the "chemical availability" of plasmonic heat in gold nanostructures. *Abstr. Pap. Am. Chem. Soc.* **2012**, *244*.
(27) Jauffred, L.; Samadi, A.; Klingberg, H.; Bendix, P. M.; Oddershede, L. B. Plasmonic Heating of Nanostructures. *Chem. Rev.* **2019**, *119*, 8087−8130.
(28) Govorov, A. Conversion of light energy into heat and hot electrons using hybrid nanostructures with plasmonic hot spots. *Abstr. Pap. Am. Chem. Soc.* **2018**, *256*.
(29) Baffou, G.; Quidant, R.; Girard, C. Heat generation in plasmonic nanostructures: Influence of morphology. *Appl. Phys. Lett.* **2009**, *94*, 153109.
(30) Richardson, H. H.; Carlson, M. T.; Tandler, P. J.; Hernandez, P.; Govorov, A. O. Experimental and theoretical studies of light-to-heat conversion and collective heating effects in metal nanoparticle solutions. *Nano Lett.* **2009**, *9*, 1139−1146.
(31) Harris, N.; Ford, M. J.; Cortie, M. B. Optimization of plasmonic heating by gold nanospheres and nanoshells. *J. Phys. Chem. B* **2006**, *110*, 10701−10707.
(32) Un, I. W.; Sivan, Y. Parametric study of temperature distribution in plasmon-assisted photocatalysis. *Nanoscale* **2020**, *12*, 17821−17832.
(33) Un, I.-W.; Sivan, Y. Size-dependence of the photothermal response of a single metal nanosphere. *J. Appl. Phys.* **2019**, *126*, 173103.
(34) Kamarudheen, R.; Aalbers, G. J.; Hamans, R. F.; Kamp, L. P.; Baldi, A. Distinguishing among all possible activation mechanisms of a plasmon-driven chemical reaction. *ACS Energy Lett.* **2020**, *5*, 2605−2613.
(35) Dubi, Y.; Sivan, Y. "Hot" electrons in metallic nanostructures-non-thermal carriers or heating? *Light Sci. Appl.* **2019**, *8*, 89.
(36) Dubi, Y.; Un, I.-W.; Sivan, Y. Distinguishing Thermal from Nonthermal ("Hot") Carriers in Illuminated Molecular Junctions. *Nano Lett.* **2022**, *22*, 2127−2133.
(37) Baffou, G.; Bordacchini, I.; Baldi, A.; Quidant, R. Simple experimental procedures to distinguish photothermal from hot-carrier processes in plasmonics. *Light: Sci. Appl.* **2020**, *9*, 108.
(38) Sivan, Y.; Baraban, J.; Un, I. W.; Dubi, Y. Comment on "Quantifying hot carrier and thermal contributions in plasmonic photocatalysis". *Science* **2019**, *364*, No. eaaw9367.
(39) Dubi, Y.; Un, I. W.; Sivan, Y. Thermal effects−an alternative mechanism for plasmon-assisted photocatalysis. *Chem. Sci.* **2020**, *11*, 5017−5027.
(40) Jain, P. K. Taking the Heat Off of Plasmonic Chemistry. *J. Phys. Chem. C* **2019**, *123*, 24347−24351.
(41) Li, X.; Zhang, X.; Everitt, H. O.; Liu, J. Light-induced thermal gradients in ruthenium catalysts significantly enhance ammonia production. *Nano Lett.* **2019**, *19*, 1706−1711.
(42) Mascaretti, L.; Schirato, A.; Montini, T.; Alabastri, A.; Naldoni, A.; Fornasiero, P. Challenges in temperature measurments in gas-phase photothermal catalysis. *Joule* **2022**, *6*, 1727−1732.
(43) Baibakov, M.; Wenger, J. Laser-induced fluorescence quenching of red fluorescent dyes with green excitation: Avoiding artifacts in PIE-FRET and FCCS analysis. *Chem. Phys. Lett.* **2018**, *706*, 669−674.
(44) Jiang, Q.; Rogez, B.; Claude, J.-B.; Baffou, G.; Wenger, J. Temperature measurement in plasmonic nanoapertures used for optical trapping. *ACS Photonics* **2019**, *6*, 1763−1773.
(45) Del Rosal, B.; Sun, C.; Loufakis, D. N.; Lu, C.; Jaque, D. Thermal loading in flow-through electroporation microfluidic devices. *Lab Chip* **2013**, *13*, 3119−3127.
(46) Honda, M.; Saito, Y.; Smith, N. I.; Fujita, K.; Kawata, S. Nanoscale heating of laser irradiated single gold nanoparticles in liquid. *Opt. Express* **2011**, *19*, 12375−12383.
(47) Park, S.; Yeon, G. J.; Lee, H.; Shin, H.-H.; Kim, Z. H. Self-Referenced SERS Thermometry of Molecules on a Metallic Nanostructure. *J. Phys. Chem. C* **2022**, *126*, 451−458.
(48) Baffou, G.; Kreuzer, M.; Kulzer, F.; Quidant, R. Temperature mapping near plasmonic nanostructures using fluorescence polarization anisotropy. *Opt. Express* **2009**, *17*, 3291−3298.
(49) Xie, X.; Cahill, D. G. Thermometry of plasmonic nanostructures by anti-Stokes electronic Raman scattering. *Appl. Phys. Lett.* **2016**, *109*, 183104.

https://doi.org/10.1021/acscatal.4c06841
ACS Catal. 2025, 15, 2359−2366

(50) Carattino, A.; Caldarola, M.; Orrit, M. Gold nanoparticles as absolute nanothermometers. *Nano Lett.* **2018**, *18*, 874−880.
(51) Jaque, D.; Vetrone, F. Luminescence nanothermometry. *Nanoscale* **2012**, *4*, 4301−4326.
(52) Chen, K.; Wang, H. Origin of Superlinear Power Dependence of Reaction Rates in Plasmon-Driven Photocatalysis: A Case Study of Reductive Nitrothiophenol Coupling Reactions. *Nano Lett.* **2023**, *23*, 2870−2876.
(53) Golubev, A. A.; Khlebtsov, B. N.; Rodriguez, R. D.; Chen, Y.; Zahn, D. R. Plasmonic heating plays a dominant role in the plasmon-induced photocatalytic reduction of 4-nitrobenzenethiol. *J. Phys. Chem. C* **2018**, *122*, 5657−5663.
(54) Keller, E. L.; Frontiera, R. R. Ultrafast nanoscale Raman thermometry proves heating is not a primary mechanism for plasmon-driven photocatalysis. *ACS Nano* **2018**, *12*, 5848−5855.
(55) Huang, J.; et al. Plasmon-induced optical control over dithionite-mediated chemical redox reactions. *Faraday Discuss.* **2019**, *214*, 455−463.
(56) Huang, B.; et al. Coreduction methodology for immiscible alloys of CuRu solid-solution nanoparticles with high thermal stability and versatile exhaust purification ability. *Chem. Sci.* **2020**, *11*, 11413−11418.
(57) Un, I. W.; Dubi, Y.; Sivan, Y. Photothermal nonlinearity in plasmon-assisted photocatalysis. *Nanoscale* **2022**, *14*, 5022−5032.
(58) Touloukian, Y.; Kirby, R.; Taylor, R.; Desai, P. D. *Thermo-Physical Properties of Matter*; Plenum Press: New York, 1975.
(59) Shaddix, C. *Proceedings of the 33rd National Heat Transfer Conference NHTC'99*; American Society of Mechanical Engineers: New York, NY, US, 1999.
(60) Kamarudheen, R.; Kumari, G.; Baldi, A. Plasmon-driven synthesis of individual metal@semiconductor core@shell nanoparticles. *Nat. Commun.* **2020**, *11*, 3957.
(61) Parmigiani, F.; Pacchioni, G.; Illas, F.; Bagus, P. S. Studies of the Cu-O bond in cupric oxide by X-ray photoelectron spectroscopy and ab initio electronic structure models. *J. Electron Spectrosc. Relat. Phenom.* **1992**, *59*, 255−269.
(62) Kasmi, A.; Arshad, M.; Waqas, M.; Monguen, C.; Azar, F.; Wu, L.-N.; Tian, Z.-Y. Insights into catalytic oxidation mechanism of CO over Cu catalyst: experimental and modeling study. *Mater. Res. Bull.* **2023**, *166*, 112343.
(63) Marimuthu, A.; Zhang, J.; Linic, S. Tuning selectivity in propylene epoxidation by plasmon mediated photo-switching of Cu oxidation state. *Science* **2013**, *339*, 1590−1593.
(64) Rice, K.; Walker, E. J.; Stoykovich, M. P.; Saunders, A. E. Solvent-dependent surface plasmon response and oxidation of copper nanocrystals. *J. Phys. Chem. C* **2011**, *115*, 1793−1799.
(65) Sekhon, J. S.; Verma, S. S. Cu, CuO, and Cu2O Nanoparticle Plasmons for Enhanced Scattering in Solar Cells. In *Renewable Energy and the Environment, OSA Technical Digest (CD)*; Optica Publishing Group, 2011; p JWE22.
(66) Robatjazi, H.; Zhao, H.; Swearer, D. F.; Hogan, N. J.; Zhou, L.; Alabastri, A.; McClain, M. J.; Nordlander, P.; Halas, N. J. Plasmon-induced selective carbon dioxide conversion on earth-abundant aluminum-cuprous oxide antenna-reactor nanoparticles. *Nat. Commun.* **2017**, *8*, 27.

https://doi.org/10.1021/acscatal.4c06841
ACS Catal. 2025, 15, 2359−2366